Research Article | Vol. 26, No. 15 | 23 Jul 2018 | OPTICS EXPRESS 19420

Optics EXPRESS

Multi-frequency differential absorption LIDAR system for remote sensing of CO_2 and H_2O near 1.6 μm

GERD A. WAGNER[1,2] AND DAVID F. PLUSQUELLIC[1,*]

[1]*Quantum Electromagnetics Division, Physical Measurement Laboratory, National Institute of Standards and Technology, Boulder, Colorado 80305, USA*
[2]*gerd.wagner@uni-hohenheim.de*
**david.plusquellic@nist.gov*

Abstract: The specifications and performance of a ground-based differential absorption LIDAR (light detection and ranging) system (DIAL) using an optical parametric oscillator (OPO) are presented. The OPO is injection-seeded with the output of a confocal filter cavity at frequencies generated by an electro-optic phase modulator (EOM) from a fixed-frequency external cavity diode laser (ECDL). The number of seed frequencies, frequency spacings, and duration is controlled with an arbitrary waveform generator (AWG) driving the EOM. Range resolved data are acquired using both photon current and photon counts from a hybrid detection system. The DIAL measurements are performed using a repeating sequence of 10 frequencies spanning a range of 37.5 GHz near 1602.2 nm to sequentially sample CO_2 and H_2O at 10 Hz. Dry air mixing ratios of CO_2 and H_2O with a resolution of 250 m and an averaging time of 10 min resulted in uncertainties as low as 6 μmol/mol (ppm) and 0.44 g/kg, respectively. Simultaneous measurements using an integrated path differential absorption (IPDA) LIDAR system and *in situ* point sensor calibrated to WMO (World Meteorological Organization) gas standards are conducted over two 10 hr nighttime periods to support traceability of the DIAL results. The column averaged DIAL mixing ratios agree with the IPDA LIDAR results to within the measured uncertainties for much of two measurement periods. Some of the discrepancies with the *in situ* point sensor results are revealed through trends observed in the gradients of the range resolved DIAL data.

OCIS codes: (280.1910) DIAL, differential absorption lidar; (280.0280) Remote sensing and sensors.

References and links

1. G. G. Gimmestad, "Differential-Absorption Lidar for Ozone and Industrial Emissions," Ch. 7 in *LIDAR: range-resolved optical remote sensing of the atmosphere*, C. Weitkamp, ed. (Springer, 2005), pp. 187–212.
2. G. Ehret, P. Bousquet, C. Pierangelo, M. Alpers, B. Millet, J. Abshire, H. Bovensmann, J. Burrows, F. Chevallier, P. Ciais, C. Crevoisier, A. Fix, P. Flamant, C. Frankenberg, F. Gibert, B. Heim, M. Heimann, S. Houweling, H. Hubberten, P. Jöckel, K. Law, A. Löw, J. Marshall, A. Agusti-Panareda, S. Payan, C. Prigent, P. Rairoux, T. Sachs, M. Scholze, and M. Wirth, "MERLIN: A French-German Space Lidar Mission Dedicated to Atmospheric Methane," Remote Sens. **9**(10), 1052 (2017).
3. Mission Experts Division, "WALES – Water Vapour Lidar Experiment in Space," in *ESA SP-1279(3) Reports for Mission Selection*, B. Battrick, ed. (ESA Publication Division, 2004).
4. M. Wirth, A. Fix, P. Mahnke, H. Schwarzer, F. Schrandt, and G. Ehret, "The airborne multi-wavelength water vapor differential absorption lidar WALES: system design and performance," Appl. Phys. B **96**(1), 201–213 (2009).
5. T. F. Refaat, U. N. Singh, J. Yu, M. Petros, S. Ismail, M. J. Kavaya, and K. J. Davis, "Evaluation of an airborne triple-pulsed 2 μm IPDA lidar for simultaneous and independent atmospheric water vapor and carbon dioxide measurements," Appl. Opt. **54**(6), 1387–1398 (2015).
6. G. Han, H. Xu, W. Gong, X. Ma, and A. Liang, "Simulations of a multi-wavelength differential absorption lidar method for CO_2 measurement," Appl. Opt. **56**(30), 8532–8540 (2017).
7. J. B. Abshire, H. Riris, C. J. Weaver, J. Mao, G. R. Allan, W. E. Hasselbrack, and E. V. Browell, "Airborne measurements of CO_2 column absorption and range using a pulsed direct-detection integrated path differential absorption lidar," Appl. Opt. **52**(19), 4446–4461 (2013).
8. J. B. Abshire, A. K. Ramanathan, H. Riris, G. R. Allan, X. Sun, W. E. Hasselbrack, J. Mao, S. Wu, J. Chen, K. Numata, S. R. Kawa, M. Y. M. Yang, and J. DiGangi, "Airborne measurements of CO_2 column concentrations made with a pulsed IPDA lidar using a multiple-wavelength-locked laser and HgCdTe APD detector," Atmos. Meas. Tech. **11**(4), 2001–2025 (2018).

#332684 https://doi.org/10.1364/OE.26.019420
Journal © 2018 Received 29 May 2018; revised 9 Jul 2018; accepted 10 Jul 2018; published 17 Jul 2018

9. U. N. Singh, T. F. Refaat, S. Ismail, K. J. Davis, S. R. Kawa, R. T. Menzies, and M. Petros, “Feasibility study of a space-based high pulse energy 2 µm CO_2 IPDA lidar,” Appl. Opt. **56**(23), 6531–6547 (2017).
10. Y. Shibata, C. Nagasawa, and M. Abo, “Development of 1.6 µm DIAL using an OPG/OPA transmitter for measuring atmospheric CO_2 concentration profiles,” Appl. Opt. **56**(4), 1194–1201 (2017).
11. G. A. Wagner and D. F. Plusquellic, “Ground-based, integrated path differential absorption LIDAR measurement of CO_2, CH_4, and H_2O near 1.6 µm,” Appl. Opt. **55**(23), 6292–6310 (2016).
12. K. Ertel, H. Linné, and J. Bösenberg, “Injection-seeded pulsed Ti:sapphire laser with novel stabilization scheme and capability of dual-wavelength operation,” Appl. Opt. **44**(24), 5120–5126 (2005).
13. A. Fix, C. Büdenbender, M. Wirth, M. Quatrevalet, A. Amediek, C. Kiemle, and G. Ehret, “Optical parametric oscillators and amplifiers for airborne and spaceborne active remote sensing of CO_2 and CH_4,” Proc. SPIE **8182**, 818206 (2011).
14. K. Numata, J. R. Chen, S. T. Wu, J. B. Abshire, and M. A. Krainak, “Frequency stabilization of distributed-feedback laser diodes at 1572 nm for lidar measurements of atmospheric carbon dioxide,” Appl. Opt. **50**(7), 1047–1056 (2011).
15. E. Cadiou, D. Mammez, J.-B. Dherbecourt, G. Gorju, J. Pelon, J.-M. Melkonian, A. Godard, and M. Raybaut, “Atmospheric boundary layer CO_2 remote sensing with a direct detection LIDAR instrument based on a widely tunable optical parametric source,” Opt. Lett. **42**(20), 4044–4047 (2017).
16. G.-W. Truong, K. O. Douglass, S. E. Maxwell, R. D. van Zee, D. F. Plusquellic, J. T. Hodges, and D. A. Long, “Frequency-agile, rapid scanning spectroscopy,” Nat. Photonics **7**(7), 532–534 (2013).
17. K. O. Douglass, S. E. Maxwell, G.-W. Truong, R. D. van Zee, J. R. Whetstone, J. T. Hodges, D. A. Long, and D. F. Plusquellic, “Rapid scan absorption spectroscopy using a waveform-driven electro-optic phase modulator in the 1.6–1.65 µm region,” J. Opt. Soc. Am. B **30**(10), 2696–2703 (2013).
18. K. W. Busch and M. A. Busch, “Cavity-Ringdown Spectroscopy,” ACS Symposium Series **720** (1999).
19. R. W. P. Drever, J. L. Hall, F. V. Kowalski, J. Hough, G. M. Ford, A. J. Munley, and H. Ward, “Laser phase and frequency stabilization using an optical resonator,” Appl. Phys. B **31**(2), 97–105 (1983).
20. A. V. Smith and D. J. Armstrong, “Nanosecond optical parametric oscillator with 90° image rotation: design and performance,” J. Opt. Soc. Am. B **19**(8), 1801–1814 (2002).
21. D. J. Armstrong and A. V. Smith, “150-mJ 1550-nm KTA OPO with good beam quality and high efficiency,” Proc. SPIE **5337**, 71–80 (2004).
22. K. O. Douglass, S. E. Maxwell, D. F. Plusquellic, J. T. Hodges, R. D. van Zee, D. V. Samarov, and J. R. Whetstone, “Construction of a high power OPO laser system for differential absorption LIDAR,” Proc. SPIE **8159**, 1–9 (2011).
23. I. E. Gordon, L. S. Rothman, C. Hill, R. V. Kochanov, Y. Tan, P. F. Bernath, M. Birk, V. Boudon, A. Campargue, K. V. Chance, B. J. Drouin, J.-M. Flaud, R. R. Gamache, J. T. Hodges, D. Jacquemart, V. I. Perevalov, A. Perrin, K. P. Shine, M.-A. H. Smith, J. Tennyson, G. C. Toon, H. Tran, V. G. Tyuterev, A. Barbe, A. G. Császár, V. M. Devi, T. Furtenbacher, J. J. Harrison, J.-M. Hartmann, A. Jolly, T. J. Johnson, T. Karman, I. Kleiner, A. A. Kyuberis, J. Loos, O. M. Lyulin, S. T. Massie, S. N. Mikhailenko, N. Moazzen-Ahmadi, H. S. P. Müller, O. V. Naumenko, A. V. Nikitin, O. L. Polyansky, M. Rey, M. Rotger, S. W. Sharpe, K. Sung, E. Starikova, S. A. Tashkun, J. V. Auwera, G. Wagner, J. Wilzewski, P. Wcisło, S. Yu, and E. J. Zak, “The HITRAN2016 molecular spectroscopic database,” J. Quant. Spectrosc. Radiat. Transf. **203**, 3–69 (2017).
24. R. K. Newsom, D. D. Turner, B. Mielke, M. Clayton, R. Ferrare, and C. Sivaraman, “Simultaneous analog and photon counting detection for Raman lidar,” Appl. Opt. **48**(20), 3903–3914 (2009).
25. NOAA, NASA, and USAF, “U.S. Standard Atmosphere,” (1976).
26. D. F. Plusquellic, O. Votava, and D. J. Nesbitt, “Absolute frequency stabilization of an injection-seeded optical parametric oscillator,” Appl. Opt. **35**(9), 1464–1472 (1996).
27. T. D. Raymond, W. J. Alford, A. V. Smith, and M. S. Bowers, “Frequency shifts in injection-seeded optical parametric oscillators with phase mismatch,” Opt. Lett. **19**(19), 1520–1522 (1994).
28. C. Kiemle, G. Ehret, A. Giez, K. J. Davis, D. H. Lenschow, and S. P. Oncley, “Estimation of boundary layer humidity fluxes and statistics from airborne differential absorption lidar (DIAL),” J. Geophys. Res. **102**(D24), 29189–29203 (1997).
29. D. H. Lenschow, V. Wulfmeyer, and C. Senff, “Measuring second- through fourth-order moments in noisy data,” J. Atmos. Ocean. Technol. **17**(10), 1330–1347 (2000).
30. S. M. Spuler, K. S. Repasky, B. Morley, D. Moen, M. Hayman, and A. R. Nehrir, “Field-deployable diode-laser-based differential absorption lidar (DIAL) for profiling water vapor,” Atmos. Meas. Tech. **8**(3), 1073–1087 (2015).
31. D. Sakaizawa, C. Nagasawa, T. Nagai, M. Abo, Y. Shibata, M. Nakazato, and T. Sakai, “Development of a 1.6 µm differential absorption lidar with a quasi-phase-matching optical parametric oscillator and photon-counting detector for the vertical CO_2 profile,” Appl. Opt. **48**(4), 748–757 (2009).
32. C. Nagasawa, M. Abo, Y. Shibata, T. Nagai, and M. Tsukamoto, “Direct detection 1.6 µm DIAL for measurements of CO_2 concentration profiles in the troposphere,” Proc. SPIE **8182**, 81820G (2011).
33. F. Gibert, D. Edouart, C. Cénac, F. Le Mounier, and A. Dumas, “2-µm Ho emitter-based coherent DIAL for CO_2 profiling in the atmosphere,” Opt. Lett. **40**(13), 3093–3096 (2015).
34. X. Sun, J. B. Abshire, J. D. Beck, P. Mitra, K. Reiff, and G. Yang, “HgCdTe avalanche photodiode detectors for airborne and spaceborne lidar at infrared wavelengths,” Opt. Express **25**(14), 16589–16602 (2017).

35. A. Dumas, J. Rothman, F. Gibert, D. Édouart, G. Lasfargues, C. Cénac, F. L. Mounier, J. Pellegrino, J. P. Zanatta, A. Bardoux, F. Tinto, and P. Flamant, "Evaluation of a HgCdTe e-APD based detector for 2 µm CO_2 DIAL application," Appl. Opt. **56**(27), 7577–7585 (2017).

1. Introduction

Differential absorption LIDAR (DIAL) and integrated path differential absorption (IPDA) LIDAR systems for atmospheric remote sensing are based on the frequency switching between an "online" frequency where absorption occurs by the molecule of interest and an "offline" frequency having negligible absorption in the atmosphere. Using these data, the evaluation of the DIAL equation [1] and IPDA LIDAR equation [2] enables the determination of range-resolved concentrations and column-integrated concentrations of the molecule, respectively.

DIAL and IPDA LIDAR systems for remote sensing of carbon dioxide (CO_2) or water vapor (H_2O) are currently under development and operation by several research institutes and national agencies for ground-based and airborne studies and as demonstrators for future spaceborne missions. The systems have typically operated with two frequencies (online, offline). More recently, however, IPDA LIDAR and DIAL systems employing more than two frequencies have been proposed and demonstrated. One reason for employing multiple frequencies is to be able to measure a molecule under different atmospheric conditions and concentrations by covering a wide range of optical thickness [3,4]. Another reason is the measurement of the concentration of a second molecule [5]. Additionally, it was demonstrated [6] that non-uniform frequency sampling of the absorption line and subsequent lineshape fits to obtain a concentration can improve the overall precision compared to DIAL measurements at two frequencies. From recent IPDA LIDAR work, some of the most sensitive retrievals reported to date have made use of 15 to 30 different frequencies across the line of interest [7,8]. Additional CO_2 IPDA LIDAR studies have been reported for the 2 µm region [5,9] and considerable 2 point CO_2 DIAL work was demonstrated near 1.6 µm [10].

A comparison of the specifications and performance of current CO_2 DIAL or H_2O DIAL and IPDA LIDAR systems have been published in detail elsewhere, e.g., see Table 1 of [11]. Here, we focus on the presentation of a multi-frequency DIAL method for simultaneous range-resolved detection of CO_2 and H_2O and provide the specifications of this system.

The multi-frequency methods for DIAL and IPDA LIDAR systems to date are based on electro-optic switching of the injection-seeding (IS) lasers [12], fiber-optical micro-electro-mechanical systems for switching of multiple IS lasers [4,13], switching and modulation of multiple IS lasers using fiber-optic Mach-Zehnder modulators and cascaded fiber couplers [14], fast current tuning of a single IS laser [7,8], or piezo-electric transducer (PZT) controlled cavity length [15]. Our approach uses a single ECDL which is electro-optically modulated (EOM) and filtered. This fast-scan method was introduced in [16,17] and deployed in an IPDA LIDAR system [11]. Here, we use this same method to demonstrate injection seeding of an OPO with a repeating sequence of 10 frequencies across a 37.5 GHz region and to specify the DIAL system performance.

One goal is to simultaneously probe CO_2 and H_2O concentrations to extract dry air mixing ratios. A second objective of this approach is to reduce systematic errors (biases) associated with seed-signal frequency shift and baseline differences in the instrumental frequency response. A third purpose is to evaluate biases in the range averaged DIAL data through comparisons with IPDA LIDAR and *in situ* point sensor measurements performed simultaneously in a localized region of the atmosphere. The over-arching objective of the multiple platform approach is to monitor dry-air CO_2 mixing ratios at the percent level with a range resolution of 250 m in 10 min intervals at 1 km range. Since H_2O concentrations typically impact CO_2 concentrations at the 10% level or less, the targeted uncertainties for H_2O are 10-fold higher. The CO_2 sources of interest include localized emissions from power plants and within area sources such as landfills, agriculture sites, and cities. A second goal is to cross validate the precision and accuracy of a portable, high-repetition-rate fiber-amplifier-based DIAL system under development. In the near term, a position scannable platform for the DIAL system is near completion to measure the emission flux from power plants and the city of Boulder (CO, USA) when coupled with wind profile measurements.

This paper is structured as follows. Section 2 introduces the overall multi-frequency CO_2-H_2O-DIAL system setup and the EOM sideband seeded OPO. Section 3 explains the multi-frequency DIAL theory and post-processing of the data. A statistic and systematic error budget analysis is given in Section 4. In Section 5, the simultaneous measurements of dry air mixing ratios obtained using an IPDA LIDAR system and a commercial point sensor based on cavity ring-down technology [18] are compared with the CO_2-H_2O-DIAL results. A summary with conclusions is provided in Section 6.

2. Multi-frequency DIAL setup

The ground-based multi-frequency CO_2-H_2O-DIAL system is depicted on the right side of Fig. 1. The left side of Fig. 1 shows the IPDA LIDAR system [11] with an additional *in situ* point sensor (CRD) and a weather transmitter (Weather TX) to compare the DIAL results with the IPDA LIDAR. We first describe the multi-frequency CO_2-H_2O-DIAL setup and then provide key specifications of the IPDA LIDAR system [11] for comparison below.

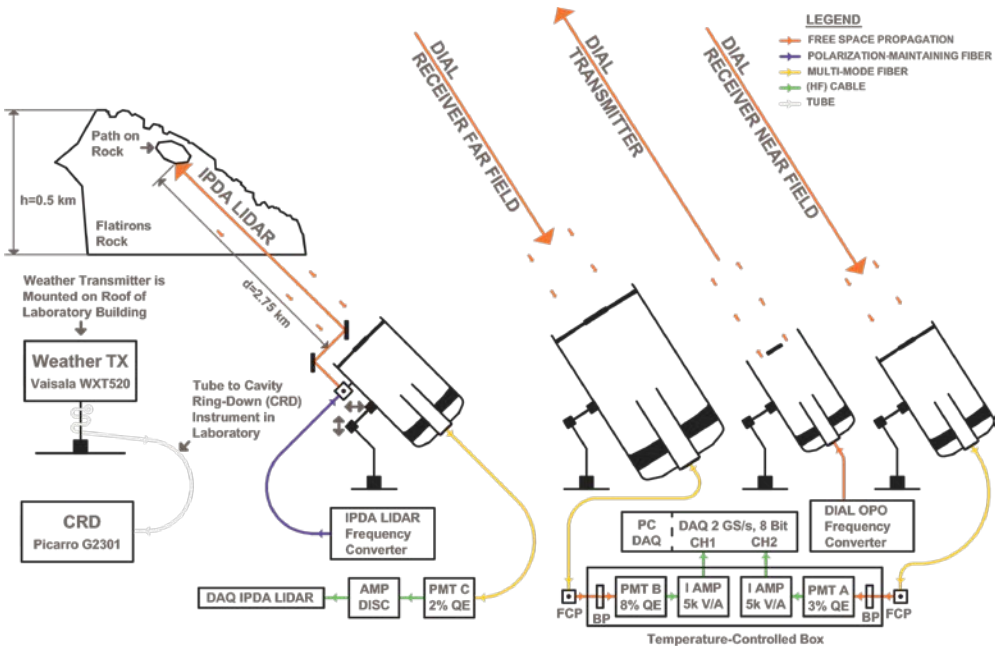

Fig. 1. Schematic sketch (not to scale) of the CO_2-H_2O-DIAL system (right side) and overall measurement setup including the IPDA LIDAR, cavity ring-down instrument (CRD), and weather transmitter (Weather TX) (left side). Right side: OPO DIAL transmitter telescope with near-field and far-field receiver telescopes with fiber-coupled (FCP) photomultiplier tube detectors (PMT A, PMT B) in temperature-stabilized box. 2 channel (CH1, CH2) data acquisition (PC DAQ) with 8 bits resolution for photon current and photon counting at a sampling rate of 2 GS/s. QE: quantum efficiency, BP: bandpass, I AMP: transimpedance amplifier (5,000 V/A gain). See Table 1 for detailed CO_2-H_2O-DIAL specifications. Left side: IPDA LIDAR transmitter-receiver telescope with detector (PMT C), amplifier-discriminator module (AMP DISC), and data acquisition (DAQ IPDA LIDAR). The cavity ring-down instrument is located in the laboratory and samples ambient air through a tube with the inlet next to the weather transmitter mounted on the laboratory roof top.

The multi-frequency CO_2-H_2O-DIAL system consists of a frequency converter (EOM-seeded OPO) with transmitter telescope, a near- and far-field receiver telescope with photomultiplier tube (PMT) detectors, and a data acquisition system for photon counting and photon current detection. Table 1 lists the specifications of the CO_2-H_2O-DIAL system.

Table 1. Specifications of CO_2-H_2O-DIAL[a]

OPO frequency converter		
Center wavelength	1602.2 nm	-
Number of frequencies	10	$\Delta\nu$ = 37.5 GHz
PRF, SRF	100 Hz, 10 Hz	limited by pump laser
Pulse energy	7 mJ	at E_p = 165 mJ
Pulse length	3 ns (FWHM)	-
Linewidth	190 MHz (FWHM)	-
Spectral purity	>99.9%	at E_p = 165 mJ
Transmitter telescope		
Diameter	258 mm	Ritchey-Chrétien, Orion
Elevation	18.4°	-
Receiver telescopes		-
Near field: diameter, FOV	279.4 mm, ≈3 mrad	Schmidt-Cassegrain, Celestron
Far field: diameter, FOV	406.5 mm, ≈2 mrad	Schmidt-Cassegrain, Meade
Detectors		
Near field: PMT	3% QE	Hamamatsu H10330A-75
Far field: PMT	8% QE	Hamamatsu H10330A-75 SEL
Bandpass filter	2 nm (FWHM), T>90%	Materion
Data acquisition		
Transimpedance amp. gain	5,000 V/A	Femto HCA-400M-5K-C
Digitizer	8 bits, 2 GS/s (0.5 ns)	GaGe CobraMax CSE24G8
Raw data storage	10 s averages	NetCDF4 file format
Range resolution	250 m	CO_2-H_2O-DIAL data product
Time resolution	10 min	CO_2-H_2O-DIAL data product

[a]$\Delta\nu$: scan tuning range, PRF: pulse repetition frequency, SRF: scan repetition frequency, E_p: pump pulse energy, FWHM: full width at half maximum, FOV: field of view, PMT: photomultiplier tube, QE: quantum efficiency, T: peak transmission. Linewidth measured using heterodyne technique. Spectral purity determined using a scanning Fabry-Perot interferometer.

The injection-seed system and the OPO design are shown in the upper and lower section of Fig. 2, respectively. The ECDL laser is split between the IPDA LIDAR (discussed below) and the OPO seed systems. For the OPO system, one leg of the fiber splitter is further amplified and tunable sidebands are added for frequency scans using a waveform generator. Single sidebands are selected and transmitted through a high finesse filter cavity. The higher finesse of this cavity relative to that of the IPDA LIDAR system cavity improves the spectral purity and increases the cavity time constant. However, this poses no timing restrictions for frequency switching of the OPO at a pulse repetition frequency (PRF) of 100 Hz. The other fiber leg is used to lock the ECDL to the filter cavity using a Pound-Drever-Hall (PDH) stabilization technique [19]. The output of the filter cavity has a carrier and non-resonant sideband rejection ratio of >30 dB which is specified using an optical spectrum analyzer (ANDO AQ6370D).

The available seed power for the OPO is ≈4 mW. The KTA OPO is based on an image rotating design (RISTRA) [20,21] and pumped with the fundamental wavelength of a Nd:YAG laser. The performance of the OPO is demonstrated in [22] and specifications relevant to this work are listed in Table 1. The idler and any residual parasitic conversion of the OPO are filtered using a prism beam separator. The near-Gaussian shaped OPO output beam is transformed into a ring mode using an axicon pair followed by a single lens to mode match to the transmitting telescope.

Optics EXPRESS

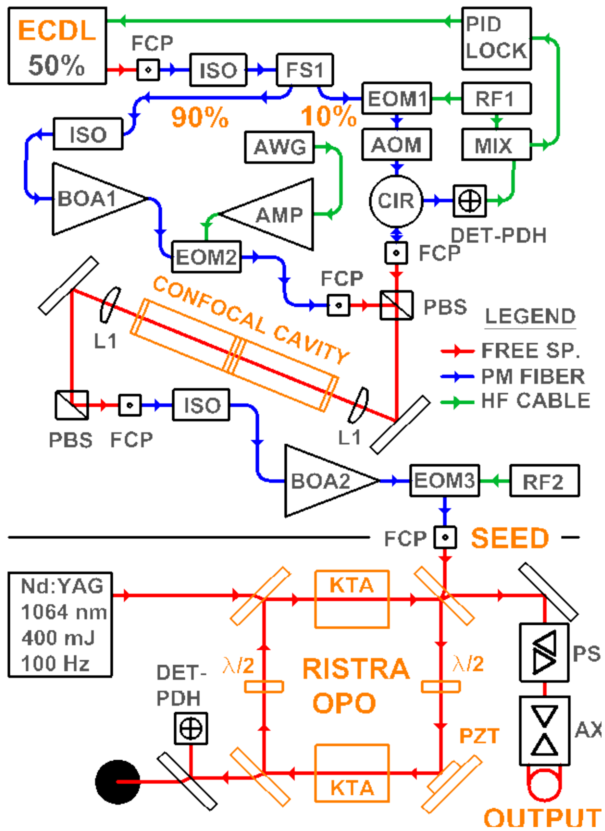

Fig. 2. Filter cavity seed system (top) and RISTRA OPO (bottom) [20,21]. The external cavity diode laser (ECDL) is fiber coupled (FCP), isolated (ISO) and split in fiber (FS1) into two legs. The 90% leg is amplified and passed through an electro-optic modulator (EOM2), free-space coupled through a polarizing beam cube (PBS), mode matched to a pressure sealed confocal filter cavity made of Invar (0.5 m long, 99% mirror reflectivity, finesse ≈600, linewidth 0.5 MHz, time constant ≈260 ns) with lens (L1), and coupled back into a PM fiber. EOM2 is driven with the amplified output (AMP) of an arbitrary waveform generator (AWG, 20 GHz, Keysight M8195A). After amplification (BOA2), 240 MHz sidebands (RF2) are added with EOM3 for OPO cavity locking before being free-space coupled into the two crystal Potassium Titanyl Arsenate (KTA) RISTRA OPO pumped with a Nd:YAG laser (Coherent Infinity 40-100, PRF: 100 Hz). The idler, pump and other parasitic conversion are spatially removed using a folded prism beam separator (PS) and the signal wave is converted to a ring mode using an axicon pair (AX) for efficient coupling through the transmitter. The second 10% leg is used for frequency locking the ECDL to the filter cavity and is first coupled through EOM1, shifted by 50 MHz in an acoustic optic modulator (AOM), passed through a circulator (CIR) and free-space combined on PBS. The reflected light is detected on a photodiode (DET-PDH) and fed back (PID) to the ECDL after mixing (MIX) the electrical signal with the local oscillator (RF1: 3 MHz) and conditioning the error signal using proportional-integral-differential electronics (PID lock).

The IPDA LIDAR system [11] is shown on the left side of Fig. 1 and key specifications are listed in Table 2. The EOM sideband based scan system is similar in design to the OPO seed system shown in Fig. 2. The IPDA LIDAR samples across 37.5 GHz with 123 frequencies at a SRF of 10 kHz. The faster scan rate requires the use of a lower finesse filter cavity (finesse ≈44, linewidth 7 MHz, carrier and residual sideband rejection ratio of 23 dB). The IPDA LIDAR system operates at an average output power of 10 mW after passing through a 2 nm bandpass filter. The reference detector power is obtained from a 5% fiber splitter port after the filter and is continuously measured on a 150 MHz photodiode. The powers across each of the 123 frequencies are first leveled from iterative adjustments of the

Optics EXPRESS

AWG waveform to within a few percent and used for normalization of the retrieved signals. Since the ECDL that seeds the IPDA LIDAR system is already locked to the OPO filter cavity, feed back to a PZT in the IPDA LIDAR filter cavity is made to correct for thermal drift.

Table 2. Key specifications of IPDA LIDAR system[a]. See [11] for details.

IPDA LIDAR frequency converter		
Center wavelength	1602.2 nm	-
Number of frequencies	123	300 MHz spacing, $\Delta\nu$ = 37.5 GHz
PRF, SRF	1.23 MHz, 10 kHz	limited by filter cavity
Pulse energy	8 nJ	output power ≈10 mW
Pulse length	600 ns	pseudo-square pulse
Linewidth	<1 MHz	transform limited
Spectral purity	>99.5%	ASE background
Transmitter		
Diameter	30 mm	-
Elevation	10.5°	-
Receiver telescope		
Diameter	279.4 mm	Schmidt-Cassegrain, Celestron
Detector		
PMT	≈1.9% QE	Hamamatsu H12397-75
Data acquisition		
Digitizer	16 bits, 200 MS/s (5 ns)	GaGe Razor CSE1622
Raw data storage	1 s averages	NetCDF4 file format
Range resolution	2.75 km	CO_2-H_2O IPDA LIDAR data product
Time resolution	30 s	CO_2-H_2O IPDA LIDAR data product-

[a]$\Delta\nu$: scan tuning range, PRF: pulse repetition frequency, SRF: scan repetition frequency, ASE: amplified spontaneous emission, PMT: photomultiplier tube, QE: quantum efficiency.

3. Multi-frequency DIAL theory and data processing

The 10 frequency points ν_1 ... ν_{10} used in the DIAL measurements are shown in Fig. 3 and are switched at a rate of 100 Hz to give a 10 Hz scan repetition frequency of the sequence. One-half of the points (ν_3 ... ν_7) are chosen near the peak optical depth of the CO_2 line to preserve most of the signal-to-noise ratio (SNR) associated with 2-point DIAL. Two (ν_8, ν_9) of the remaining 5 points are selected to sample near the peak optical depth of two different H_2O lines. The three remaining points (ν_1, ν_2, ν_{10}) are chosen at two different off-resonance regions near the two edges of the scan. The timing sequence is chosen to sequentially sample in the low-to-high ν order shown in Fig. 3. In this way, the three baseline points are sequentially sampled and therefore enable the removal in first order of any residual instrument frequency response (see below).

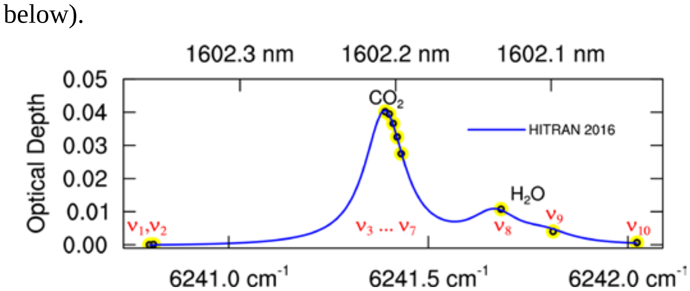

Fig. 3. Sample line shape fit using HITRAN2016 [23] to the sampled points, ν_1 ... ν_{10}, of the CO_2-H_2O-DIAL system. The optical depth is shown for a 10 min average and 500 m path length (250 m range bin) at 1 km range. The peak optical depth of 0.04 corresponds to a fractional absorption of ≈4%.

Optics EXPRESS

The photon current and photon count data for all 10 frequencies are processed using a temporal average of 1 min (6 profiles). The pulse pileup (saturation) parameter for each PMT is first determined from non-linear least squares fits of clear sky data up to 4 km for the two nighttime runs. The saturation-corrected photon count data are then least squares fit to photon current data for each 1 min profile using a scalar and offset. These parameters are then inverted to adjust the photon current data to effective counts as previously discussed [24]. In the high-count signal region, the cross over region fit was restricted to a maximum from 40 million to 50 million counts per second (CPS) after which saturation corrections to our non-paralyzable detection system start to become invalid. The cut-off in the low-count region is restricted to rates no less than 10 CPS to 15 CPS because of the limited 8-bit resolution of the digitizer. Typically, the fit region corresponds to a range from 2.4 km to 4 km, below which the corrected photon current data is spliced in. Effective count rates, N, in excess of 2×10^9 CPS are observed near the peak of the retrievals and decreased geometrically with range to a background count rate of 3×10^5 CPS (for the PMT with 8% QE).

The observed optical depth A at range $R = (R_1 + R_2)/2$, with range resolution $\Delta R = (R_2\text{-}R_1)$ and frequency ν_i is defined according to

$$A(R,\nu_i) = \ln\left[\frac{N_i(R_1)N_b(R_2)}{N_b(R_1)N_i(R_2)}\right], \tag{1}$$

where N_b is arbitrarily chosen as the first offline point with $A(R, \nu_1) = 0$. The optical depths $A(R, \nu_i)$ are fit to a Voigt line shape $V(R, \nu_i)$ that includes the linewidth corrected cross sections σ_m of each species m taken from HITRAN2016 [23],

$$V(R,\nu_i) = 2\Delta R \sum_m \sigma_m(R,\nu_i), \tag{2}$$

σ_m is based on the *in situ* temperature and pressure measurements after correction for altitude using the U.S. Standard Atmosphere model [25] and includes a contribution from the spectral distribution of the laser. As detailed in our previous IPDA LIDAR work [11], only the two group absorption intensities of CO_2 and H_2O are varied in the fits together with an offset and baseline slope. The fits give concentration in µmol/mol (ppm) for CO_2 and percent mol/mol for H_2O for a given range. For the fits, the center frequency is fixed for the altitude at the fitted value to the average of the first 10 range bins to eliminate systematic errors associated with the observed OPO seed/signal shift [26,27] of 100-130 MHz relative to the IPDA LIDAR center frequencies. The center frequency uncertainties from the fits are typically less than ± 10 MHz. A sample line shape fit is illustrated in Fig. 3 taken from a 10 min average over the first range bin of the far-field data at 1 km.

For the IPDA LIDAR retrievals, the optical depth of the CO_2 line over the 5.5 km path is ≈0.43 which gives roughly 35% fractional absorption. As discussed elsewhere [11], the data were first corrected for a small amount of amplified spontaneous emission (which is 5 times less than previously reported in [11] because of the 5-fold narrower bandpass filter), normalized to reference power and converted to optical depth. The measured profile for each 30 s average (300,000 scans) is fit to a Voigt lineshape based on HITRAN2016 [23]. The Voigt lineshape is obtained from the average over 3 equally spaced range bins for the 500 m elevation of the IPDA LIDAR beam using the U.S. Standard Atmosphere model [25] relative to the *in situ* temperature and pressure data measured at the base. For each 30 s interval, the same parameters that were fit in the DIAL measurements were varied here but also included the center frequency. The center frequency uncertainties are typically less than ± 20 MHz in 30 s. Furthermore, the maximum center frequency drift over the duration of the 10 hr period is also ± 20 MHz and reflects the absolute frequency stability of the OPO Invar filter cavity to which the seed laser is locked. The fit of a baseline slope and offset removes to first order the spectral dependence of the retrievals relative to the leveled output powers. At 10 min

Optics EXPRESS

measurement intervals, the Allan deviations of the CO_2 dry air mixing ratios are 2 ppm to 3 ppm for both nighttime runs and similar to our previous results [11].

4. Error budget analysis

DIAL, IPDA and point sensor measurements were performed over two 10 hour nighttime periods on 11/29/2017 and 11/30/2017. As detailed below, measurement uncertainties for 250 m range resolution were evaluated for the first night based on the Allan deviations, the autocovariance function [28,29] and the average of the standard deviations of the fits. Similar metrics of system performance were found for the second night.

Allan deviations of the CO_2 fitted number densities at 10 s intervals for 3 different ranges are depicted in Fig. 4(a) for the 10 hour period. The trends follow the expected improvement with root averaging time out to about 10 min at 1 km, 30 min at 2 km and over the full night at 3 km. As illustrated in the concentration maps discussed below, the natural changes in the mixing ratios that occur during the measurement period lead to the upward turn of these curves at the shorter ranges. For 10 min averaging times, the relative uncertainties of CO_2 mixing ratios are 1.5%, 3.6%, and 6.0% and of H_2O are 11%, 25%, and 42% at 1 km, 2 km, and 3 km ranges, respectively. Figure 4(b) shows the autocovariance function for the same time series at 1 km range for 10 s and 10 min lags. The 10 min lag results show similar contributions from uncorrelated (natural) variance and signal (instrumental) variance.

A more direct measure of the instrumental statistical noise component on the 10 min time scale is obtained from the root-mean-square of the fit standard deviations (RMS SDs). Figure 4(c) shows the overnight RMS SDs (type A, $k = 1$ or $1\ \sigma$) for CO_2 and H_2O as a function of range. The data follow the expected quadratic increase with increasing range and indicate a precision of ≈0.5% for CO_2 and ≈4% for H_2O at 1 km range in 10 minutes. Unlike the Allan deviations which are based on the fluctuations of the fitted concentrations over all time scales longer than the 10 sec minimum, the fit SDs measure the uncertainty for each 10 min interval and therefore, contain no information about the natural fluctuations of concentration across the 10 min intervals. At 1 km, the RMS SD of 0.5% for CO_2 gives a measure of the instrumental noise component shown in the 10 min auto-covariance function of Fig. 4(b). As expected, this value is less than the Allan deviation of 1.5% which includes a significant contribution from natural CO_2 fluctuations. Furthermore, the Allan deviation is larger than the DIAL random error estimate [30] of ≈1% when the total accumulated counts from all 5 online points are taken into account indicating further improvement in performance will require the use of higher pulse energy and/or a higher PRF.

Optics EXPRESS

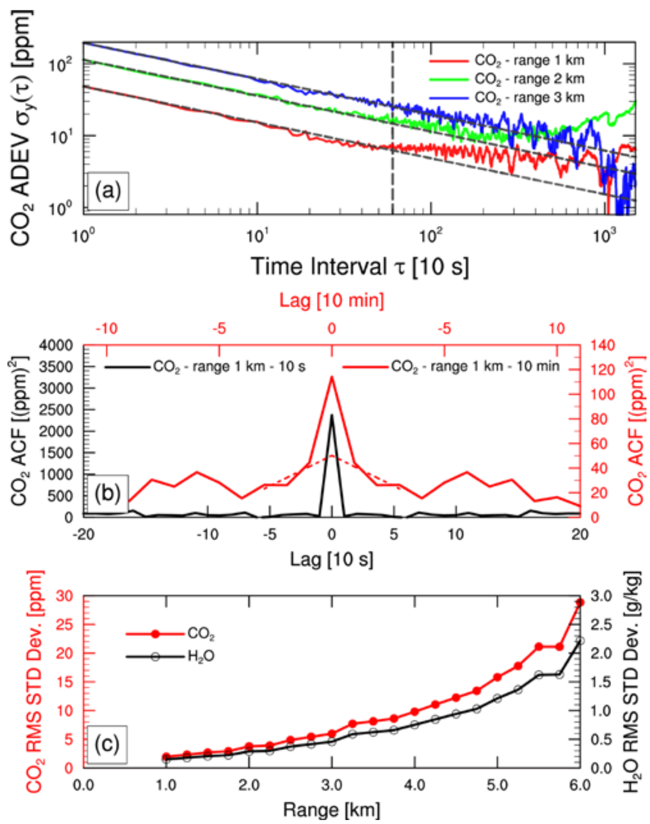

Fig. 4. (a) Allan deviations (ADEV) of CO_2 DIAL data obtained at 250 m resolution and at 10 s measurement intervals, (b) autocovariance function (ACF) of CO_2 mixing ratio at 1 km range with dashed lines showing the 3-point linear fits for extrapolation to zero lag to estimate uncorrelated and signal variance, (c) the root mean square (RMS) of the 10 min fit standard deviations of CO_2 and H_2O.

Table 3 lists error sources contributing to the total error budget of the multi-frequency DIAL measurements. The error sources are divided into five main categories and include errors due to (1) the detection system (e.g., statistical and baseline), (2) the OPO frequency converter, (3) the underlying spectroscopic database and lineshape model, (4) the uncertainty of the weather transmitter data, and (5) atmospheric variations of temperature and pressure along the measurement path. In summary, the most significant errors are associated with the statistical noise in the returns, the spectroscopic database and lineshape model, the signal wave frequency uncertainty, and temperature variations over the beam path. We estimate a conservative measurement bias (systematic error) of 1% to 2% for CO_2 concentrations in our measurements.

A comparison of our measurement sensitivity with a 2 frequency DIAL measurement using a periodically poled $LiNbO_3$ OPO system operating at 110 Hz near 1572 nm [31] shows similar sensitivity in the 3 km to 5 km range after a ≈15-fold adjustment of uncertainties for averaging time (× 5.5) and range resolution (× 2.8). A comparison with the second generation 2 frequency OPA/OPG DIAL system [32] operating at 500 Hz and 10.3 W is more difficult but appears to have roughly 3-fold larger uncertainties at 4.5 km than reported here following a 30-fold adjustment for averaging time (× 2) and range (× 15). An additional comparison with the 2 frequency CO_2 DIAL heterodyne measurement [33] at 2.051 μm with 10-fold higher average power shows similar uncertainties within comparable averaging intervals.

Optics EXPRESS

Table 3. Statistic and systematic error budget of CO_2-H_2O-DIAL

Error source	Uncertainty	Measurement error	Comment
Detection system			
Statistical noise in returns	≈1%	-	10 min av., 250 m range bin
PMT dark photon current	<0.04%	negligible	EMI corrected; 8 bit DAQ
PMT dark photon counts	<0.01%	negligible	amplifier, discriminator
PMT spectral response	<0.1%	negligible	baseline slope fit
Fit standard deviation CO_2	-	≈0.5%	at 1 km, 10 min; Fig. 4(c)
Fit standard deviation H_2O	-	≈4.0%	at 1 km, 10 min; Fig. 4(c)
Speckle effect	-	negligible	see [11] for IPDA LIDAR
OPO frequency converter			
Seed frequency stability	± 15 MHz	not relevant	using DIAL center fit data
Signal frequency stability	± 10 MHz	± 0.3%	-
Power stability	≈4%	not relevant	DIAL ratio insensitive
Spectral impurity	<0.1%	± 0.05%	spectral purity >99.9%
Overall spectral response	-	not relevant	DIAL ratio insensitive
Electrical stability	-	negligible	transimpedance amplifier
Spectroscopy			
HITRAN 2016: CO_2	(1-2)%	-	lineshape fit
HITRAN 2016: H_2O	(5-10)%	-	lineshape fit
Voigt lineshape model	≈1%	-	-
Weather TX sensor			
Temperature	± 0.3 K	negligible	Vaisala WXT520
Pressure	± 0.5 hPa	negligible	Vaisala WXT520
Atmosphere			
Path length	± 0.15 m	± 0.06%	250 m range bin
Temperature	± 3 K	± 0.6%	two local weather stations
Pressure	± 1.5 hPa	± 0.03%	two local weather stations

5. Simultaneous multi-platform measurements

Figures 5 and 6 show the merged near- and far-field DIAL measurements for the 11/29/2017 and 11/30/2017 nighttime runs, respectively. Dry air CO_2 and H_2O mixing ratios are depicted in panels Fig. 5(a), Fig. 6(a), and Fig. 5(b), Fig. 6(b), respectively. The data are shown for an effective time resolution of 10 min and for linearly increasing range resolution beginning near 250 m for < 1 km range to about 1 km resolution above 5 km. The IPDA LIDAR beam path heights are near the top of the mountain and indicated with dashed gray horizontal lines in Figs. 5[(a), (b), (e)] and Figs. 6[(a), (b), (e)]. Range-corrected backscatter data (offline, ν_1) of the far-field system are shown in the lower panels (Fig. 5(e), Fig. 6(e)).

On the night of 11/29/2017 (Fig. 5(e)), the top of the boundary layer is near ≈2 km and above our measurement range throughout the night with, however, an additional layer appearing near the top of the mountain at 0.5 km. Above and below this lower layer, the CO_2 and H_2O mixing ratios shown in panel Fig. 5(a) are seen to undergo changes of up to 20-30 ppm for CO_2 and ≈2.0 g/kg for H_2O. Furthermore, this layer is seen to descend over the course of the night more slowly for CO_2 than for H_2O. For the night-time data of 11/30/2017 shown in Fig. 6(a), less distinct but similar changes are seen in mixing ratio, but in this case, the transition occurs at longer range that is closer to but still below the top of the boundary layer.

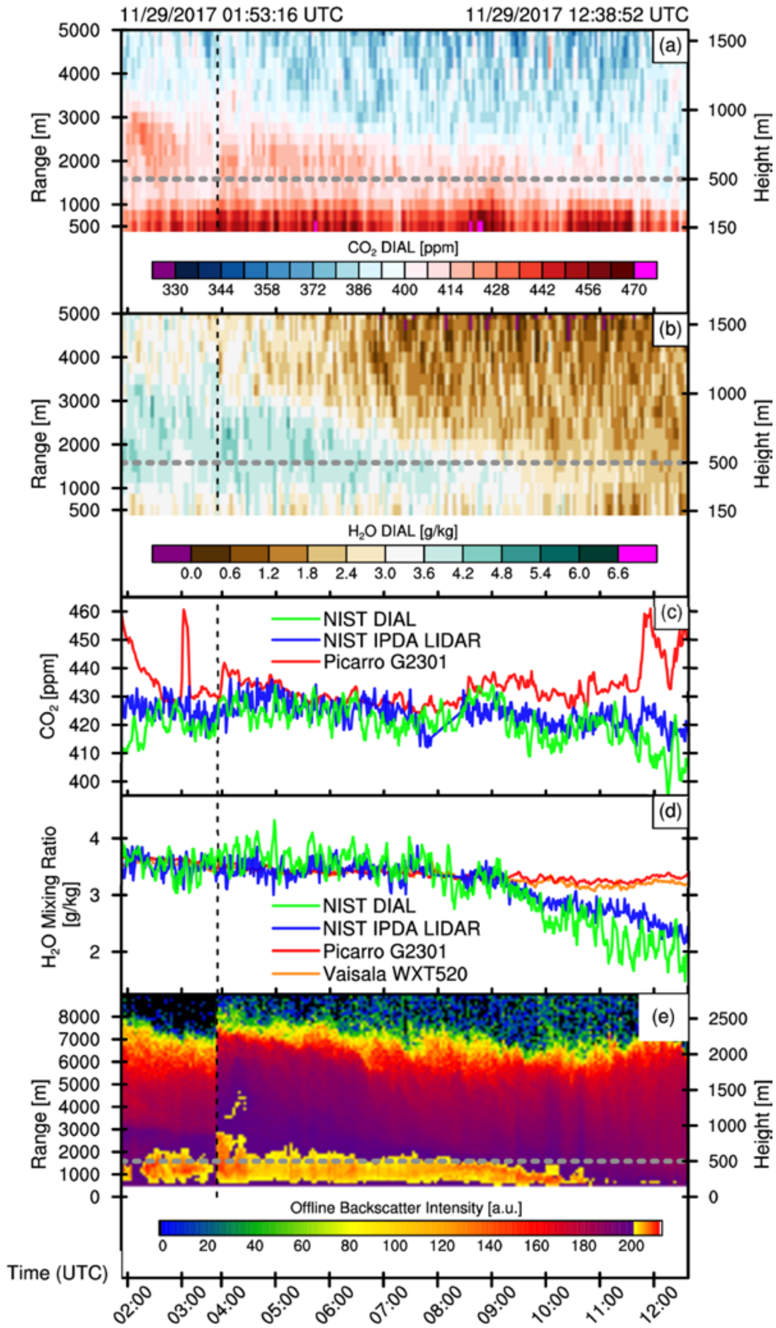

Fig. 5. DIAL measurements on 11/29/2017 consisting of the (a) range resolved CO_2, (b) range resolved H_2O dry air mixing ratios, and (e) range and background corrected offline (ν_1) backscatter signals. Comparisons of the IPDA LIDAR and point sensor data (Picarro G2301 and Vaisala WXT520) are made with the column averaged DIAL data (0.5 km to 1.75 km) for (c) CO_2 and (d) H_2O, respectively. DIAL surfaces are shown for an effective time resolution of 10 min and for increasing range bin size (see text for details). Dashed vertical line indicates a small gap in data. Time on abscissa is UTC (local time −7 hrs).

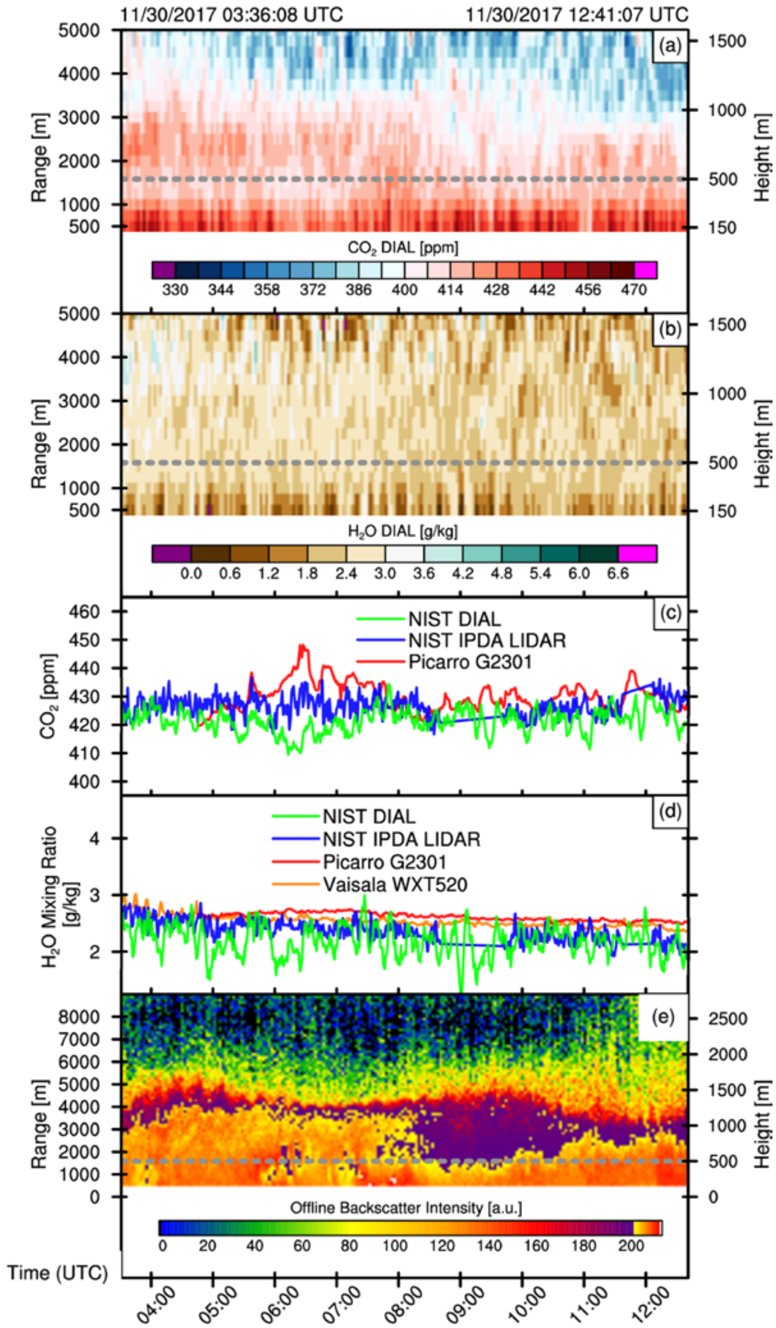

Fig. 6. Multi-platform measurements on 11/30/2017. A description follows that of Fig. 5.

The column averages of the CO_2 and H_2O mixing ratios are determined for the DIAL data from 0.5 km out to 1.75 km range, the latter of which corresponds to the height of the IPDA LIDAR beam. The column averages are evaluated at a range resolution of 250 m and for an effective time resolution of 5 min. In Figs. 5 and 6, these data are compared with the IPDA LIDAR and point sensor dry-air mixing ratios in panels Fig. 5(c), Fig. 6(c), and Fig. 5(d), Fig. 6(d), respectively. (For the second night, the Picarro data for the first 2.5 hrs. are missing because of a problem with the acquisition software). Particularly for the first night, the large gradients of CO_2 concentrations detected by the point sensor are not captured by the IPDA LIDAR and column averaged DIAL data. The change in the CO_2 mixing ratio with the descending layer shown in Fig. 5(a) may partially account for the mixing ratio differences.

The H_2O DIAL data in Fig. 5(d) are in good agreement with the IPDA LIDAR and point sensor data up until 9:00 UTC where DIAL and the IPDA LIDAR data decrease relative to the point sensor data. After 9:00 UTC, the fraction of the IPDA LIDAR beam path sampling dryer air is seen to increase while the point sensors sample the higher levels below this layer throughout the night. For both nights, the CO_2 point sensor data is slightly higher than the IPDA and DIAL data which may result from extrapolation of the slightly decreasing gradient with increasing range seen beyond the initial 0.5 km of missing DIAL data.

Figure 7 shows the mean CO_2 mixing ratio for each 250 m range bin for both measurements runs (Fig. 5(a), Fig. 6(a)). For the 11/29/2017 measurement, the Allan deviations at 10 min intervals are added at 1 km increments (red bars). The averages over all times and range bins are 398 ppm and 400 ppm for the first and second night, respectively.

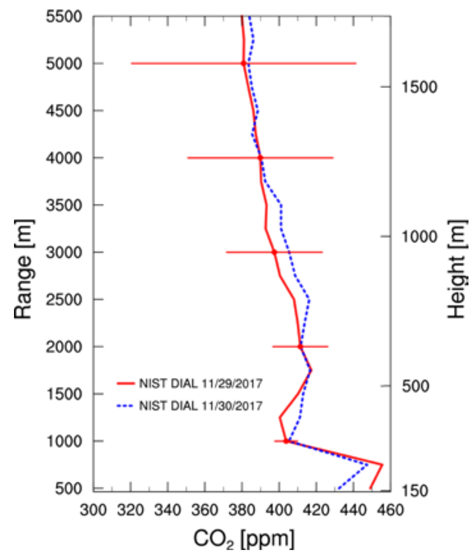

Fig. 7. Mean CO_2 profile for DIAL measurements of 11/29/2017 (Fig. 5(a)) and 11/30/2017 (Fig. 6(a)). Uncertainties for measurement of 11/29/2017 determined from the Allan deviations for 10 min intervals and 250 m range resolution are shown with horizontal bars.

6. Conclusions

In summary, the multi-frequency output from an AWG-EOM based filter-cavity system is used for injection-seeding an OPO for ground-based 10-point DIAL measurements of CO_2 and H_2O dry air mixing ratios. We have specified measurement precision relative to the instrumental and natural fluctuations of the measurements and the uncertainties based on the Allan deviation and RMS standard deviations of the fits. These analyses indicate for a 250 m range bin at 1 km and 10 min averaging time a measurement precision of 6 µmol/mol (ppm) and 0.44 g/kg for CO_2 and H_2O which are near 1.5% and 11% of the ambient levels, respectively. Accompanying IPDA LIDAR and WMO traceable *in situ* point sensor measurements are in good agreement with the 0.5 km to 1.75 km column average of the DIAL data and suggest the accuracy and precision of the measurements are of similar magnitude.

While the current uncertainties are adequate to quantify fugitive or plume emission from stacks, improvements need to be made to reduce the statistical noise of the return signals to attain the ppm sensitivity needed for emission flux measurements from distributed area sources. The KTA OPO (RISTRA) has been demonstrated to operate at 7 times the average

Optics EXPRESS

power used in current studies, and future studies will also benefit from a pump laser with a higher PRF. Finally, the promising developments in HgCdTe detector technology [8,34,35] could significantly improve overall system efficiency.

Funding

Special Programs Office and Physical Measurement Laboratory, NIST.

Acknowledgments

We thank Stephen Maxwell (NIST) and Kevin Douglass (NIST) for the design and construction of the prism beam separator and assembly of the OPO, Christoph Senff (CIRES/NOAA) for DIAL performance calculations, Kimberly Briggman (NIST), James Whetstone (NIST) and Adam Fleisher (NIST) for useful discussions. We also thank Darrell Armstrong (Sandia National Laboratories) for the optical design of the RISTRA OPO. Contribution of National Institute of Standards and Technology, not subject to copyright in the United States.

Certain commercial equipment, instruments, or materials are identified in this paper in order to specify the experimental procedure adequately. Such identification is not intended to imply recommendation or endorsement by NIST, nor is it intended to imply that the materials or equipment identified are necessarily the best available for the purpose.